ChemBioChem

Research Article
doi.org/10.1002/cbic.202401071

Chemistry Europe
European Chemical Societies Publishing

www.chembiochem.org

VIP *Very Important Paper*

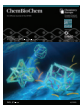

Wireframe DNA Origami Capable of Vertex-protruding Transformation

Yosuke Ochi[+],[a] Wataru Kato[+],[a] Yoichi Tsutsui[+],[a] Yuki Gomibuchi,[c] Daichi Tominaga,[b] Keisuke Sakai,[c] Takeshi Araki,[a] Suzunosuke Yoshitake,[a] Takuo Yasunaga,[c] Yusuke V. Morimoto,[c] Kazuhiro Maeda,[a] Junichi Taira,[a] and Yusuke Sato*[b]

Regulating dynamic behavior of the designed molecular structures provides a foundation for the construction of functional molecular devices. DNA nanotechnology allows conformational changes in two-dimensional and three-dimensional DNA origami nanostructures by introducing flexibility between the faces of the structures. However, dynamic transformations in wireframe DNA origami, composed solely of vertices and edges, remain challenging due to vertex-specific flexibility. We report a wireframe DNA origami capable of vertex-protruding transformation between the open- and closed-form with eight protruding vertices. This reversible transformation is driven by DNA hybridization and a toehold-mediated strand displacement reaction. Spacer strands between vertices and edges were designed to introduce flexibility. Coarse-grained molecular dynamics simulations demonstrated that a longer spacer increases conformational flexibility and can achieve the narrow angles required for the vertex-protruding transformation. The experimental results showed the successful assembly of the open-form structure under optimized salt conditions, as visualized through transmission electron microscopy images. Furthermore, the transformation between the open- and closed-form structures was demonstrated by the sequential addition of signal strands. This vertex-protruding transformation mechanism will expand the design approach of dynamic DNA nanostructures and help develop functional molecular devices for artificial molecular systems.

Introduction

Understanding the dynamic behavior of nanoscale structures is a fundamental challenge in molecular-based engineering. Natural proteins provide compelling examples of how regulated conformational changes enable key functions, such as sensing and actuating functions, in living cells, as observed in membrane receptors and motor proteins.[1,2] These biological machinery offer inspiration for designing artificial molecular devices.[3–6] Artificially engineering dynamic molecular devices requires materials with high designability and programmability at the molecular level. Achieving precise structures and dynamic motions depends on partial flexibility, a range of motion, and intermolecular interactions; these challenges stem from the need to mimic the conformational changes observed in natural proteins and design molecular devices for tailored functions.

DNA exhibits sequence-dependent self-assembly based on Watson–Crick base pairing; this property is best adopted for a programmable nanoscale material. In the field of structural DNA nanotechnology,[7,8] DNA serves as a building block for constructing various structures, and several methods such as DNA tiles[9–13] and DNA origami[14–16] have been developed as a structural assembly method. The DNA tile method designs a structural unit, which further assembles into higher order structures, whereas DNA origami uses a long single-stranded DNA (ssDNA) called a scaffold, folded into arbitrary-shaped structures including two-dimensional (2D)[14] or three-dimensional (3D),[16,17] and wireframe designs.[18–22] Thus, various dynamic DNA nanostructures were developed using the DNA origami method owing to its high designability.[23]

Many approaches for the conformational changes and transformation of DNA origami nanostructures have been proposed based on a mechanical geometry viewpoint. In 2D and 3D DNA origami, flexible hinges at the edges between two faces are often utilized, allowing for dynamic actuation, such as openable boxes[24,25] or crank-slider mechanisms.[26] Besides the flexible hinges, 3D DNA origami structures are physically bent to function as springs[27] or leaf springs.[28] Although most dynamic DNA origami designs are based on 2D or 3D shapes, a few mechanisms have been demonstrated for wireframe DNA origami.[29–31]

[a] *Y. Ochi,[+] W. Kato,[+] Y. Tsutsui,[+] T. Araki, S. Yoshitake, Prof. Dr. K. Maeda, Prof. Dr. J. Taira*
Department of Bioscience and Bioinformatics
Kyushu Institute of Technology
680-4 Kawazu, Iizuka, Fukuoka, 820-8502, Japan

[b] *D. Tominaga, Prof. Dr. Y. Sato*
Department of Intelligent and Control Systems
Kyushu Institute of Technology
680-4 Kawazu, Iizuka, Fukuoka, 820-8502, Japan
E-mail: ysato@ics.kyutech.ac.jp

[c] *Dr. Y. Gomibuchi, K. Sakai, Prof. Dr. T. Yasunaga, Prof. Dr. Y. V. Morimoto*
Department of Physics and Information Technology
Kyushu Institute of Technology
680-4 Kawazu, Iizuka, Fukuoka, 820-8502, Japan

[+] *Dedication Y. Ochi, W. Kato, and Y. Tsutsui equally contributed to this work.*

Supporting information for this article is available on the WWW under https://doi.org/10.1002/cbic.202401071

The key feature of wireframe DNA origami lies in its structural components, which are composed of only vertices and edges without faces. This unique composition renders the design of transformable wireframe origami structures particularly difficult. For example, Nayan et al. reported the shape transformation of a wireframe origami structure by enzymatic extension of its edges,[29] while Mogheiseh et al. designed a temperature-dependent actuation mechanism for a wireframe origami based on hybridization stability.[30] However, the flexible hinge approach commonly used in conventional 2D and 3D DNA origami cannot be directly applied to wireframe DNA origami. While traditional origami uses the edges between faces as flexible hinges, wireframe structures require flexibility to be introduced solely at vertices.

Here, we experimentally demonstrate a wireframe DNA origami capable of vertex-protruding transformation (hereafter referred to as WO-VPT) (Figure 1). The WO-VPT can reversibly transform between open- and closed-form structures with protruded vertices. The vertex protrusions are induced by the hybridization of ssDNAs extending from the edges (zipper strands) with the signal strands (close signal), leading to a shortened edge distance and a reduced angle between the edges connected to the vertex. The transformation from the closed- to open-form structure occurs via a toehold-mediated strand displacement reaction, which detaches the close signal. The crucial factor in this shape transformation was vertex flexibility. Coarse-grained molecular dynamics (MD) simulation confirmed the feasibility of our design approach, and the experimental result demonstrated the successful shape transformation of WO-VPT in response to each signal strand. The proposed reversible shape transformation mechanism will expand the potential applications of wireframe DNA origami nanostructures.

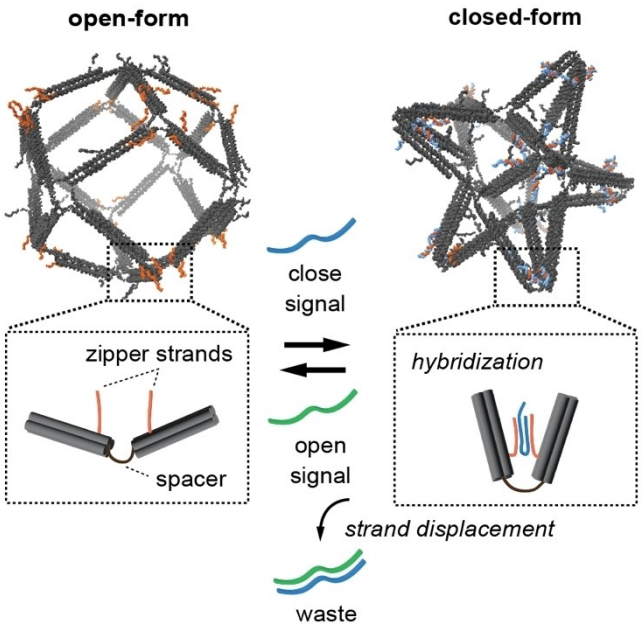

Figure 1. Schematic of the reversible transformation of wireframe DNA origami capable of vertex-protruding transformation (WO-VPT). The transformation from the open- to closed-form structure is driven by the hybridization of zipper strands extending from designated edges with the close signal. Conversely, the closed- to open-form transformation occurs via a toehold-mediated strand displacement reaction.

Results and Discussion

Structure Design and MD Simulation

The shape of the open-form WO-VPT was designed as a rhombic dodecahedron with 14 vertices (Figure 1, left). Scaffold routing was performed using a program developed by Benson et al.[32] Each edge was constructed as a four-helix bundle to enhance the rigidity.[33] Zipper strands, 17- or 18-nucleotides (nt) in length, were extended from each edge. The hybridization of the zipper strands with the close signal strands bridges the edge, transforming into the closed-form with eight protruding vertices (Figure 1, right). This transformation mechanism was designed to be reversible: the close signal hybridized with the zipper strands could be removed via a strand displacement reaction with the open signal, thereby restoring WO-VPT to its open-form structure.

For the transformation from the open- to the closed-form, each edge must move closer to allow the two zipper strands to hybridize with a single signal strand; thus, the WO-VPT must have structural flexibility. To evaluate the flexibility required for the transformation, we examined how the length of the ssDNA spacer, which connects each edge to the vertices (Figure 2a), affects the conformational flexibility. Three different structure models with spacer lengths of 3-, 6-, and 10-nt were prepared, and coarse-grained MD simulations were performed using oxDNA.[34] Notably, the maximum spacer length was limited to 10 nt owing to the scaffold length constraint.

After the equilibration (Figure S1), the conformational flexibility of each spacer length was compared using the root mean square fluctuation (RMSF) values. The histogram indicated that the longer spacers resulted in larger RMSF values (Figure 2b). This increased conformational flexibility also influenced edge mobility, as reflected in the edge distance, which was assessed based on the average angles formed between the edges and zipper strands. The angular histogram revealed that the longer spacer design exhibited smaller angle values (Figure 2c). The average angles of 3-, 6-, and 10-nt were $104.7 \pm 23.3^\circ$, $96.8 \pm 20.6^\circ$, and $90.6 \pm 27.1^\circ$, respectively. These findings suggest that the 10-nt spacer design facilitates the closest edge distance and is the most suitable for enabling the transformation. The behavior of the closed-form with 10-nt spacers was evaluated using a model with prehybridized zipper and signal strands (Figure 2d). In the closed-form, the RMSF values significantly decreased compared to the open-form (Figure 2e), indicating that the hybridization reduced the edge mobility introduced by the 10-nt spacer. Furthermore, the average angle of the edges was $50.1 \pm 17.5^\circ$ (Figure 2f), within the movable range of the open-form with the 10-nt spacer. The angular histogram showed a 36% overlap between the open- and closed-form, suggesting that the conformations accessible through the thermal fluctuations of the open-form encompass

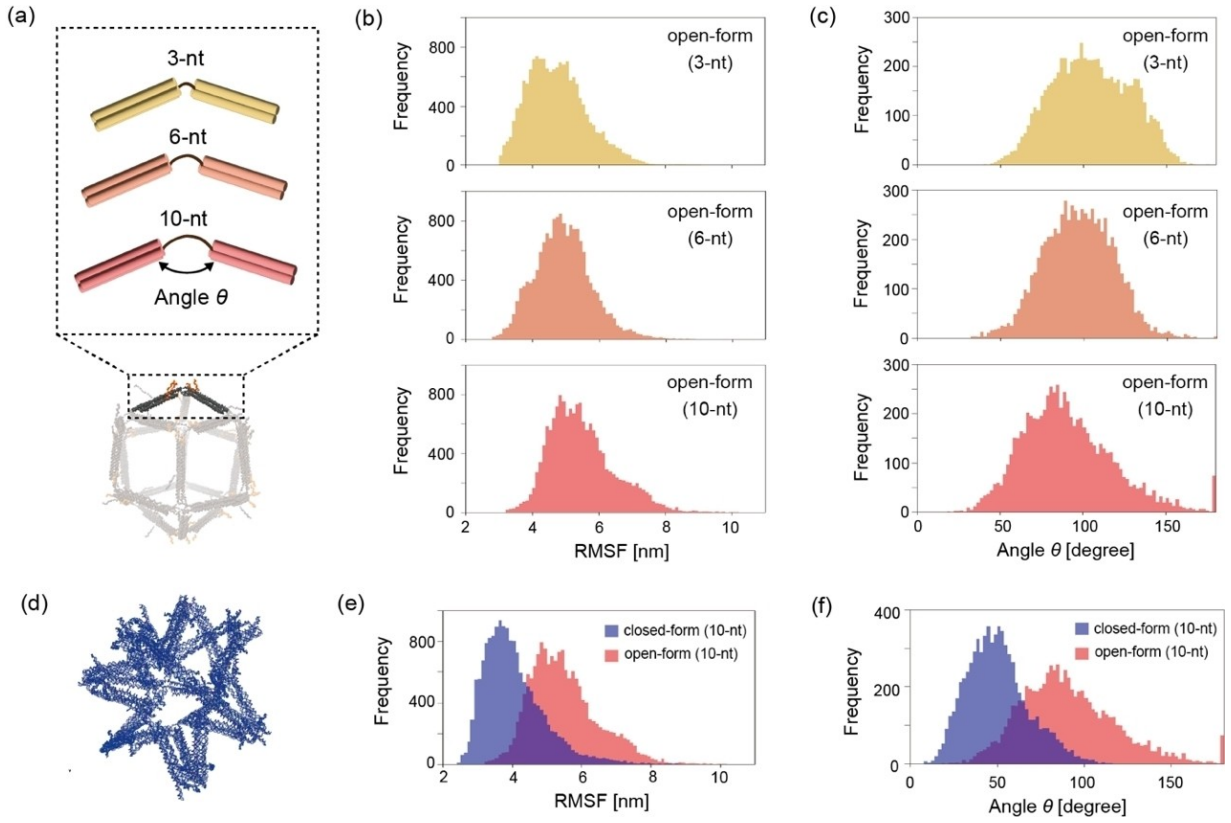

Figure 2. Analysis of the coarse-grained MD simulation of WO-VPT. (a) Differences in the spacer lengths. The angle between the two sides is expressed by θ. (b) Histograms of the RMSF values for the open-form with a spacer length of 3-nt, 6-nt, and 10-nt. (c) Histograms of the angle values for the open-form (3-nt, 6-nt, and 10-nt). (d) Average configuration of the closed-form with a 10-nt spacer. (e) Histograms of the RMSF values for the open-form with a 10-nt spacer and the closed-form. (f) Histograms of the angle values for the open- and closed-forms.

intermediate conformations during the transformation to the closed-form.

Folding of the Open-Form Wireframe Origami

Based on the insights from MD simulations, the open-form WO-VPT with 10-nt spacers was assembled through thermal annealing. Various salt conditions were tested using agarose gel electrophoresis (AGE) to optimize the assembly conditions. First, an appropriate magnesium concentration was explored by altering $MgCl_2$ concentrations ranging from 12.5–22.5 mM in 2.5 mM increments (Figure S2). However, folding with $MgCl_2$ alone as the salt did not provide conditions conducive to successful structure assembly. While less aggregation was observed at 12.5 mM and 15 mM $MgCl_2$, few structures were assembled (Figure S3). At higher $MgCl_2$ concentrations, aggregation occurred (Figure S2). We hypothesized that higher magnesium concentrations are required for the structure folding;[33] however, the increased conformational flexibility by the spacer and the salt-bridging effects of the divalent cations (Mg^{2+}) likely promoted aggregation. Thus, we added 100 mM NaCl to the folding buffer with 22.5 mM $MgCl_2$ to reduce the magnesium-mediated electrostatic interaction. Sodium ions are known to suppress the aggregation of DNA nanostructures by providing electrostatic shielding.[16] Thus, adding 100 mM NaCl reduced the aggregation (Figure S4). We also investigated different annealing ramp conditions; the longer annealing ramp (22 h) induced more aggregation than that of the short ramp (4 h) (Figure S5); hence, the short ramp was used. To confirm the correct assembly of the structure, the sample was purified using a gel extraction method[35] (Figure 3a). After purification, the sample exhibited a slight band shift in the AGE analysis, which can be attributed to differences in the ionic strength during the purification process. The purified sample was characterized using transmission electron microscopy (TEM) (Figure 3b). The TEM images showed structures composed of multiple connected squares with an average edge length of 27.3 nm, closely matching the designed edge length of 25 nm, indicating successful folding of the open-form.

Reversible Transformation between Open- and Closed-Form

The reversible transformation was confirmed through the sequential addition of each signal strand. First, the transformation to the closed-form structure was induced by adding the close signal to the open-form structure. Subsequently, the open signal was added to induce the transformation back to the open form via toehold-mediated strand displacement

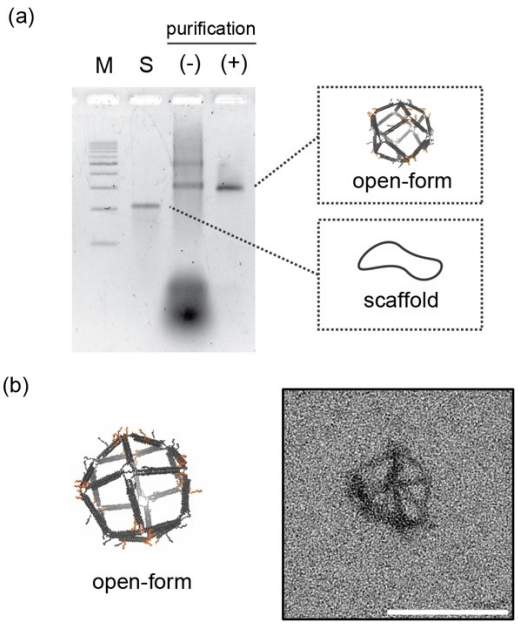

Figure 3. Construction of the open-form structure. (a) AGE of the open-form before and after gel purification. Lane M: 1 kb ladder marker; Lane S: scaffold; Lane (−) and (+): The open-form before and after purification, respectively. (b) A representative TEM image of the open-form after purification. Scale bar = 100 nm.

(Figure 4a). The hybridization between the zipper and signal strands, as well as the strand displacement reaction, were confirmed using polyacrylamide gel electrophoresis (PAGE) (Figure S6). Two types of zipper strands were prepared to avoid intra-edge connections (Figure S7). The sequences of the zipper and signal strand were designed based on a previous study.[36]

The initial transformation from the open-form to the closed-form structure was verified using AGE following the addition of the close signal followed by incubation at 25°C for 12 h. The AGE results showed a clear downward band shift (Figure 4b), suggesting a reduction in apparent structural size. The subsequent transformation from the closed- to the open-form was confirmed after the addition of the open signal and incubation at 25°C for 6 h. The AGE results displayed an upward band shift (Figure 4b), with the band aligning closely with that of the initial open-form structure.

The transformation was visualized through TEM observation. Unlike the open-form structure (Figure 4c (i) and Figure S8), the observed structure after the addition of the close signal exhibited radially extending protrusions from its center (Figure 4c (ii) and Figure S9), indicating transformation into the closed-form. Following the addition of the open signal, the TEM images showed structures resembling the initial open-form structures (Figure 4c (iii) and Figure S10), demonstrating successful reversion. The transformation yields of the intended structures at each stage – initial open-form, closed-form, and reverted open-form structures – were 19.6%, 6.4%, and 10.3%, respectively (Figure S11a). Many observed structures appeared to be damaged and could not be classified into these forms. Since AGE showed a single band (Figure 4b), we infer that structural damage likely occurred during TEM sample preparation, where samples were exposed to low-salt conditions. To account for this, we recalculated the proportion of intact structures corresponding to each intended form, excluding those that were clearly damaged. The proportions of the closed-form and reverted open-form structures were 58.8% and 81.8%, respectively (Figure S11b). The lower proportion of closed-form structures is likely due to the combined requirements of DNA hybridization and physical edge convergence, whereas reversion to the open-form occurs solely through signal DNA hybridization.

The transformation was quantified by counting the number of vertices in the observed structure due to the closed-form structure with protruding and recessed vertices (Figure 4d). The average number of outer vertices was 8.48 ± 1.48 in the initial open-form structure, decreasing to 4.47 ± 0.52 in the closed-form structure. In the reverted open-form, the count increased to 8.00 ± 1.19, closely matching the initial open-form structure and confirming successful reversion. The WO-VPT was designed with 14 vertices in the open-form and 8 protruding vertices in the closed-form, which differs from the number of outer vertices observed. This discrepancy is likely due to the 2D projection inherent in TEM images.

Conclusions

In this study, we demonstrated a novel transformation mechanism for wireframe DNA origami, characterized by its unique structural features – comprising only vertices and edges without faces – resulting in the vertex-protruding transformation from a standard wireframe origami shape (Figure 1). The key factor for this mechanism is conformational flexibility, which is achieved by introducing spacer ssDNAs between the edges and vertices, enabling the vertex-protruding transformation. The optimal spacer length favorable for the transformation was identified through coarse-grained MD simulation (Figure 2). A longer spacer length increased the likelihood of smaller interedge angles around the vertices, increasing the conformational flexibility required for the transformation. Despite this increased flexibility, the open-form wireframe origami was successfully assembled and visualized through TEM images (Figure 3). The addition of the signal strands induced the reversible transformation between the open-form and vertex-protruding closed-form (Figure 4).

While this study demonstrated the protrusion transformation of vertices induced by signal strand addition, alternative stimuli-responsive mechanisms, such as ion-responsive guanine quadruplexes,[37] pH-responsive motifs,[38,39] azobenzene photoisomerization,[40] or aptamer-based molecular recognition,[37,41] could facilitate reversible transformations in response to diverse stimuli.

The designed structure can theoretically switch between configurations where 8 of the 14 vertices protrude, and 6 are recessed, and *vice versa*. This switching capability arises from the geometrical characteristics of the dual polyhedrons. Specifically, the rhombic dodecahedron used in this study incorporates regular hexahedrons and octahedrons as their structural

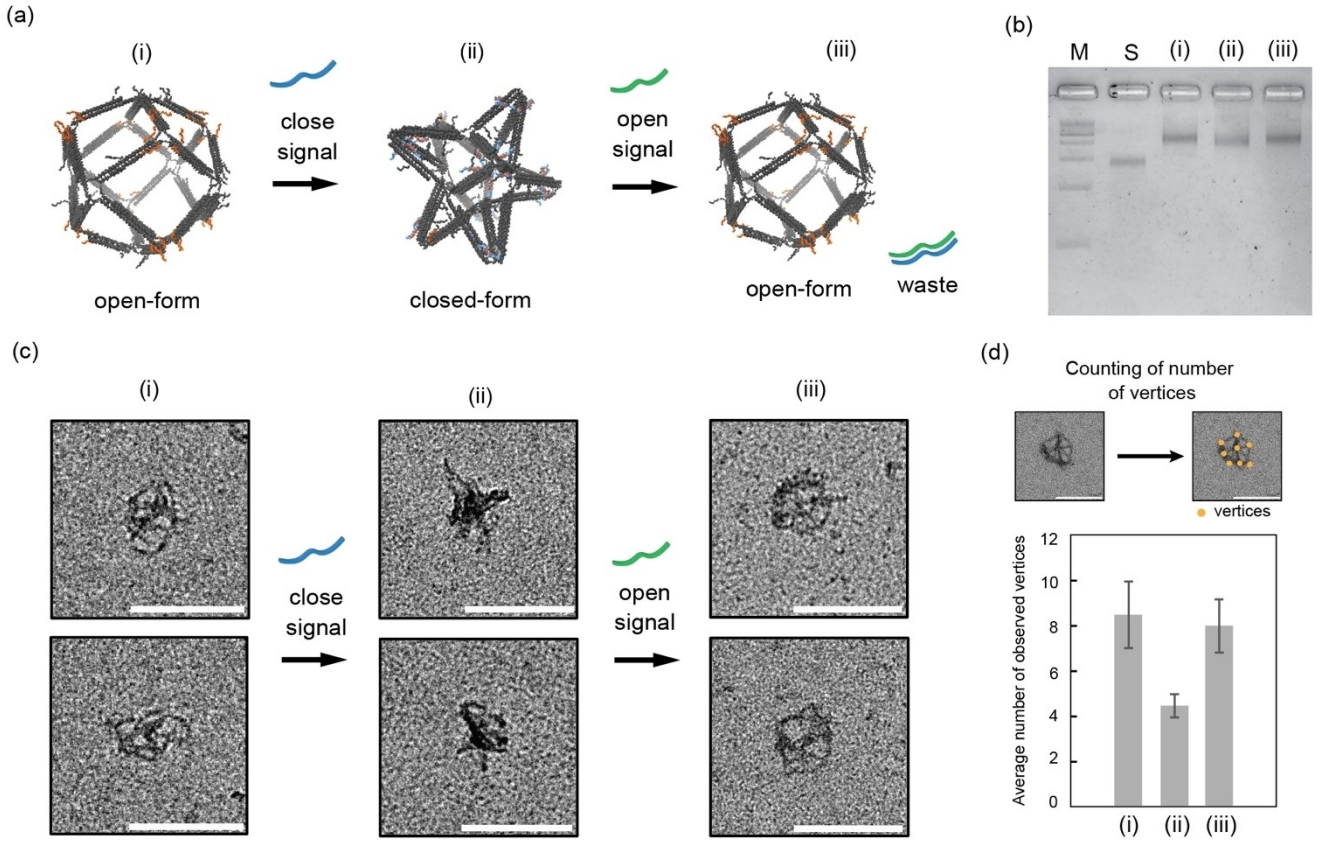

Figure 4. Reversible transformation between the open- and the closed-form structures. (a) Schematic of the reversible transformation. (b) AGE of the reversible transformation. Lane M: 1 kb ladder marker; Lane S: scaffold; Lane (i): initial open-form structure; Lane (ii): (i) closed-form structure after close-signal addition; Lane (iii): reverted open-form structure after open-signal addition. (c) Representative TEM images of (i), (ii), and (iii). (d) Comparison of the average number of observed vertices among (i) (n = 85), (ii) (n = 20), and (iii) (n = 18). Error bars represent standard deviation. Scale bars = 100 nm.

components,[42] which exhibit a duality relationship,[43] interchanging the positions of the faces and vertices; this property facilitates control over the switching between the protruding and recessed vertices (Figure S12). Such vertices-switching functionality could regulate the surface exposure of functional molecules, such as enzymes attached to the vertices,[44] offering promising potential for drug delivery carriers. We believe that the proposed transformation mechanism significantly broadens the applicable potential of wireframe DNA origami, contributing to the development of versatile molecular devices for artificial molecular systems.[45–47]

Experimental Section

Structure Design

To design the WO-VPT, an entire shape of the rhombic dodecahedron was prepared in the polygon file format (ply file). Then, the scaffold routing was designed using the beam scaffolded origami routing software (https://github.com/mohamma1/bscor),[32] which also generated the RPOLY and NTRAIL files; these files were used with the software developed by Lolaico et al.[33] to convert each edge into 4HB to increase the edges' rigidity. The generated json file was used in caDNAno software.[48,49] The positions of the zipper strands extended from the edges were decided by calculating the distance from the vertices, and the staple path and length were adjusted. The caDNAno maps of the scaffold and staples are shown in Figures S13–S16, and the sequences are shown in Tables S1 and S2.

Coarse-Grained Simulation

The structure for the simulation was obtained in the oxDNA format by converting the json file output from caDNAno using the web-based tacoxDNA (http://tacoxdna.sissa.it/).[50] Subsequently, the structure was loaded into the web-based oxView (https://oxdna.org/static/oxdna-viewer/index.html)[51] and relaxed using a rigid-body simulation. A two-step relaxation and MD simulation was subsequently performed using the local version of oxDNA. The first stage of the relaxation calculation involved a Monte Carlo simulation with 1×10^4 steps, and the second stage entailed an MD simulation with 1×10^8 steps. In the subsequent MD simulation, the oxDNA2 model was used at a temperature of 25°C, a salt concentration of 1.5 M, a thermostat set to Langevin, and a time step (dt) of 0.001, running for 3×10^8 steps. The state of the simulation was saved every 1×10^6 steps. After the simulation, the oxDNA analysis tools were used to export and calculate the average configuration, root-mean-square deviation, and RMSF.

DNA Origami Folding

The open-form was assembled in 60 μl solution containing 10 nM p7560 scaffold (Tilbit nanosystems, Germany), 100 nM staple strands (Eurofins genomics, JAPAN), 5 mM Tris-HCl (pH 8.0), 1 mM EDTA, 22.5 mM $MgCl_2$, and 100 mM NaCl. Different staple sets were used depending on the target structures (Table S3). The mixture was annealed in a thermal cycler (T One96G, Biometra, Germany) at 65°C for 15 min, from 53°C to 50°C at a rate of −1°C/min, and then the sample was stored at 4°C.

The closed-form structure was constructed by adding the close signal (Table S2). Three equivalents of the close signal relative to the zipper strand were added to the open-form structure purified by gel extraction, followed by incubation at 25 °C for 12 h. Reversion to the open-form structure was achieved by adding ten equivalents of the open signal relative to the close signal, followed by incubation at 25 °C for 6 h.

Structure Analysis and Purification by AGE

The samples were loaded onto 2.0 % agarose gel (KANTO, Japan) containing 5 mM $MgCl_2$ in 0.5× tris-borate-EDTA (TBE) buffer. As a running buffer, 0.5× TBE with 5 mM $MgCl_2$ was used. Electrophoresis was performed at 50 V for 3 h at 4°C. A 1 kb DNA ladder (TaKaRa, Japan) was used as a reference. The gel was stained with SYBR Gold (Thermo Fisher Scientific, United States) and imaged with a WSE-6100H LuminoGraph I (ATTO, Japan).

To purify WO-VPT, 1 % agarose gel (KANTO, Japan) was cast using 0.5× TBE buffer supplemented with 5 mM $MgCl_2$. As a running buffer, 0.5× TBE with 5 mM $MgCl_2$ was used. Electrophoresis was performed at 100 V for 2 h at 4°C. The gel was stained and imaged using the same method described above. For gel extraction, the gel was incubated overnight in the running buffer. The desired band was then cut out using a gel cutter, chopped, and transferred into a DNA gel extraction column (Freeze'N Squeeze DNA Gel Extraction Spin Columns, Bio-Rad, United States). The extracted gel was incubated for 5 min at –20°C and centrifuged at 13,000×*g* at 4 °C for over 20 min. Centrifugation was repeated until the filtrate stopped flowing, and the purified sample was obtained. Since the $MgCl_2$ concentration in the purified sample was approximately 5 mM, additional $MgCl_2$ solution was added to adjust the final concentration to 22.5 mM.

PAGE

Polyacrylamide gels were prepared by mixing 15 % (w/v) acrylamide-bis (29 : 1) (Nakalai Tesque, Japan), 1 % (w/v) ammonium peroxodisulfate, 0.1 % (v/v) tetramethylethylenediamine, and 5 mM $MgCl_2$ in a 0.5× TBE buffer. A solution containing 0.5× TBE with 5 mM $MgCl_2$ was used for a running buffer. Electrophoresis was performed at 100 V for 3 h at 4°C. The gel was stained with SYBR Gold (Thermo Fisher Scientific, United States) and then imaged using an imager.

TEM Imaging

Carbon-coated TEM grids (Okenshoji, Japan) underwent plasma treatment for 10 s. A 3 μL aliquot of the sample solution was deposited to the TEM grid and incubated for 5 min at room temperature. Next, the structures were stained with aqueous uranyl acetate solution (1 %(w/v)) for 5 min at room temperature. Furthermore, three washing steps were performed using ultrapure water, and the water was removed with filter paper. The samples were imaged using Tecnai G2 Spirit (FEI, United States) at 120 kV.

Acknowledgements

We thank Prof. Dr. Takashi Nakakuki for his valuable comments on the launch of this project. This work initially began as an entry in the International Biomolecular Design Competition 2023 (https://biomod.net/). This work was supported in part by MEXT/JSPS KAKENHI (Grant numbers JP20H05970, JP 23 K17860, JP24 K03034 to Y.S., JP23H04427 to J.T., and JP 22H04926 to T.Y.), JST FOREST Program (JPMJFR2344) to Y.S., and Kyutech Project for Promotion of Education to J.T.

Conflict of Interests

The authors declare no conflict of interest.

Data Availability Statement

The data that support the findings of this study are available from the corresponding author upon reasonable request.

Keywords: DNA nanostructure · Wireframe DNA origami · Transformation · oxDNA

[1] F. A. Kiani, S. Fischer, *Cytoskeleton* **2016**, *73*, 643–651.
[2] Z. Zhang, F. Liu, J. Chen, *Cell* **2017**, *170*, 483–491.e8.
[3] F.-H. Ma, C. Li, Y. Liu, L. Shi, *Adv. Mater.* **2020**, *32*, 1805945.
[4] S. Howorka, *Nat. Nanotechnol.* **2017**, *12*, 619–630.
[5] M. J. Langton, *Nat. Rev. Chem.* **2020**, *5*, 46–61.
[6] M. Liu, J. Cheng, S. R. Tee, S. Sreelatha, I. Y. Loh, Z. Wang, *ACS Nano* **2016**, *10*, 5882–5890.
[7] N. C. Seeman, *Nature* **2003**, *421*, 427–431.
[8] F. Zhang, J. Nangreave, Y. Liu, H. Yan, *J. Am. Chem. Soc.* **2014**, *136*, 11198–11211.
[9] T. H. LaBean, H. Yan, J. Kopatsch, F. Liu, E. Winfree, J. H. Reif, N. C. Seeman, *J. Am. Chem. Soc.* **2000**, *122*, 1848–1860.
[10] H. Yan, S. H. Park, G. Finkelstein, J. H. Reif, T. H. LaBean, *Science* **2003**, *301*, 1882–1884.
[11] Y. He, Y. Chen, H. Liu, A. E. Ribbe, C. Mao, *J. Am. Chem. Soc.* **2005**, *127*, 12202–12203.
[12] P. Yin, R. F. Hariadi, S. Sahu, H. M. T. Choi, S. H. Park, T. H. LaBean, J. H. Reif, *Science* **2008**, *321*, 824–826.
[13] S. Hamada, S. Murata, *Angew. Chem. Int. Ed.* **2009**, *48*, 6820–6823.
[14] P. W. K. Rothemund, *Nature* **2006**, *440*, 297–302.
[15] D. Han, S. Pal, Y. Yang, S. Jiang, J. Nangreave, Y. Liu, H. Yan, *Science* **2013**, *339*, 1412–1415.
[16] S. M. Douglas, H. Dietz, T. Liedl, B. Högberg, F. Graf, W. M. Shih, *Nature* **2009**, *459*, 414–418.
[17] D. Han, S. Pal, J. Nangreave, Z. Deng, Y. Liu, H. Yan, *Science* **2011**, *332*, 342–346.
[18] F. Zhang, S. Jiang, S. Wu, Y. Li, C. Mao, Y. Liu, H. Yan, *Nat. Nanotechnol.* **2015**, *10*, 779–784.
[19] H. Jun, F. Zhang, T. Shepherd, S. Ratanalert, X. Qi, H. Yan, M. Bathe, *Sci. Adv.* **2019**, *5*, eaav0655.
[20] W. Wang, S. Chen, B. An, K. Huang, T. Bai, M. Xu, G. Bellot, Y. Ke, Y. Xiang, B. Wei, *Nat. Commun.* **2019**, *10*, 1067.
[21] X. Wang, S. Li, H. Jun, T. John, K. Zhang, H. Fowler, J. P. K. Doye, W. Chiu, M. Bathe, *Sci. Adv.* **2022**, *8*, eabn0039.
[22] M. Kim, C. Lee, K. Jeon, J. Y. Lee, Y.-J. Kim, J. G. Lee, H. Kim, M. Cho, D.-N. Kim, *Nature* **2023**, *619*, 78–86.
[23] M. DeLuca, Z. Shi, C. E. Castro, G. Arya, *Nanoscale Horiz.* **2020**, *5*, 182–201.
[24] E. S. Andersen, M. Dong, M. M. Nielsen, K. Jahn, R. Subramani, W. Mamdouh, M. M. Golas, B. Sander, H. Stark, C. L. P. Oliveira, J. S.

Pedersen, V. Birkedal, F. Besenbacher, K. V. Gothelf, J. Kjems, *Nature* **2009**, *459*, 73–76.
[25] G. Grossi, M. Dalgaard Ebbesen Jepsen, J. Kjems, E. S. Andersen, *Nat. Commun.* **2017**, *8*, 992.
[26] A. E. Marras, L. Zhou, H.-J. Su, C. E. Castro, *Proc. Natl. Acad. Sci.* **2015**, *112*, 713–718.
[27] D. Karna, E. Mano, J. Ji, I. Kawamata, Y. Suzuki, H. Mao, *Nat. Commun.* **2023**, *14*, 6459.
[28] M. Centola, E. Poppleton, S. Ray, M. Centola, R. Welty, J. Valero, N. G. Walter, P. Šulc, M. Famulok, *Nat. Nanotechnol.* **2023**, *19*, 226–236.
[29] N. P. Agarwal, M. Matthies, B. Joffroy, T. L. Schmidt, *ACS Nano* **2018**, *12*, 2546–2553.
[30] M. Mogheiseh, R. Hasanzadeh Ghasemi, *J. Chem. Phys.* **2024**, *161*, 045101.
[31] M. Mogheiseh, R. H. Ghasemi, *Mol. Syst. Des. Eng.* **2024**, DOI 10.1039/D4ME00144C.
[32] E. Benson, A. Mohammed, J. Gardell, S. Masich, E. Czeizler, P. Orponen, B. Högberg, *Nature* **2015**, *523*, 441–444.
[33] M. Lolaico, S. Blokhuizen, B. Shen, Y. Wang, B. Högberg, *ACS Nano* **2023**, *17*, 6565–6574.
[34] E. Poppleton, M. Matthies, D. Mandal, F. Romano, P. Šulc, L. Rovigatti, *J. Open Source Softw.* **2023**, *8*, 4693.
[35] K. F. Wagenbauer, F. A. S. Engelhardt, E. Stahl, V. K. Hechtl, P. Stömmer, F. Seebacher, L. Meregalli, P. Ketterer, T. Gerling, H. Dietz, *ChemBioChem* **2017**, *18*, 1873–1885.
[36] J.-S. Shin, N. A. Pierce, *J. Am. Chem. Soc.* **2004**, *126*, 10834–10835.
[37] A. Kuzuya, Y. Sakai, T. Yamazaki, Y. Xu, M. Komiyama, *Nat. Commun.* **2011**, *2*, 449.
[38] D. Karna, M. Stilgenbauer, S. Jonchhe, K. Ankai, I. Kawamata, Y. Cui, Y.-R. Zheng, Y. Suzuki, H. Mao, *Bioconjug. Chem.* **2021**, *32*, 311–317.
[39] H. Ijäs, I. Hakaste, B. Shen, M. A. Kostiainen, V. Linko, *ACS Nano* **2019**, *13*, 5959–5967.
[40] A. Kuzyk, Y. Yang, X. Duan, S. Stoll, A. O. Govorov, H. Sugiyama, M. Endo, N. Liu, *Nat. Commun.* **2016**, *7*, 10591.
[41] S. M. Douglas, I. Bachelet, G. M. Church, *Science* **2012**, *335*, 831–834.
[42] E. W. Weisstein, "Rhombic Dodecahedron," can be found under https://mathworld.wolfram.com/RhombicDodecahedron.html, **2023** (accessed 20 December 2024).
[43] J. Y. Zhang, M. Ohsaki, F. Tsuura, *Int. J. Solids Struct.* **2019**, *161*, 182–192.
[44] J. S. Kahn, Y. Xiong, J. Huang, O. Gang, *JACS Au* **2022**, *2*, 357–366.
[45] S. Murata, in *Mol. Robot. Introd.* (Ed.: S. Murata), Springer Nature, Singapore, **2022**, pp. 1–11.
[46] Y. Sato, *ChemSystemsChem* **2024**, *6*, e202400021.
[47] N. Zhao, Y. Chen, G. Chen, Z. Xiao, *ACS Appl. Bio Mater.* **2020**, *3*, 3928–3934.
[48] C. E. Castro, F. Kilchherr, D.-N. Kim, E. L. Shiao, T. Wauer, P. Wortmann, M. Bathe, H. Dietz, *Nat. Methods* **2011**, *8*, 221–229.
[49] S. M. Douglas, A. H. Marblestone, S. Teerapittayanon, A. Vazquez, G. M. Church, W. M. Shih, *Nucleic Acids Res.* **2009**, *37*, 5001–5006.
[50] A. Suma, E. Poppleton, M. Matthies, P. Šulc, F. Romano, A. A. Louis, J. P. K. Doye, C. Micheletti, L. Rovigatti, *J. Comput. Chem.* **2019**, *40*, 2586–2595.
[51] E. Poppleton, J. Bohlin, M. Matthies, S. Sharma, F. Zhang, P. Šulc, *Nucleic Acids Res.* **2020**, *48*, e72–e72.

Manuscript received: December 27, 2024
Revised manuscript received: February 17, 2025
Accepted manuscript online: February 19, 2025
Version of record online: March 12, 2025